Theoretical Investigations on the Plasmon-Mediated Dissociation of Small Molecules in the Presence of Silver Atomic Wires

Olivia A. Hull and Christine M. Aikens*

Department of Chemistry, Kansas State University, Manhattan, KS 66506, USA

* cmaikens@ksu.edu; Phone: 1-785-532-0954

Abstract

Plasmonic nanoparticles can promote bond activation in adsorbed molecules under relatively benign conditions via excitation of the nanoparticle's plasmon resonance. As the plasmon resonance often falls within the visible light region, plasmonic nanomaterials are a promising class of catalyst. However, the exact mechanisms through which plasmonic nanoparticles activate the bonds of nearby molecules are still unclear. Herein, we evaluate Ag_8-X_2 (X = N, H) model systems via real-time time-dependent density functional theory (RT-TDDFT), linear response time-dependent density functional theory (LR-TDDFT), and Ehrenfest dynamics in order to better understand the bond activation processes of N_2 and H_2 facilitated by the presence of the atomic silver wire under excitation at the plasmon resonance energies. We find that dissociation is possible for both small molecules at high electric field strength. Activation of each adsorbate is symmetry- and electric field-dependent, and H_2 activates at lower electric field strengths than N_2. This work serves as a step towards understanding the complex time-dependent electron and electron-nuclear dynamics between plasmonic nanowires and adsorbed small molecules.

1. Introduction

Plasmonic nanoparticles (NPs) have generated significant research interest owing to their highly tunable optical properties.[1–3] These properties, and their tunability, are a direct consequence of the symmetries of the particles and the confinement effects that arise due to the nanometer length scale of these systems. Plasmonic nanoparticles find application in catalysis,[1,4–12] photovoltaics,[13–15] sensing and detection,[16–19] medicine,[20–22] and more. Photocatalysis is an area of particular interest, as plasmonic nanoparticles have been shown to activate adsorbates like O_2,[12] H_2,[7] CO_2,[8] H_2O,[10] and others.[9,11,23] Many of these adsorbates are not easily activated through

traditional means, yet experiment shows that plasmonic photocatalysis can occur under relatively benign conditions, such as room temperature and pressure and low light intensity.

Plasmonic NPs achieve this photocatalytic activity through excitation of the plasmon resonance. The plasmon resonance can be thought of as the collective oscillation of free surface electrons, which occurs at a particular plasmon resonance frequency. The plasmon resonance frequency is readily tunable based on the size and shape of the particle, among other factors. While the plasmon resonance plays an important role in plasmonic photocatalysis, the exact means of activation are not fully understood. There has been intense research effort in defining and distinguish the mechanisms through which the plasmonic particles achieve activation, but uncertainty remains.[24–27] To further obfuscate the issue, in small nanoclusters where quantum effects dominate, there are numerous ways to identify or define the plasmon resonance.[28–31] In this paper, we employ the "quantum plasmon" framework, which identifies plasmonic peaks in small clusters as coherent excitations of multiple single-particle transitions with near-equal transition coefficients as computed by linear response time-dependent density functional theory.[31,32]

Given the tunability of the plasmon resonance and the fact that the plasmon resonance plays an important role in plasmon-mediated photocatalysis, there is significant research interest in understanding exactly how the plasmon resonance affects the catalysis process, and how to harness the tunability of the resonance for this purpose.[2] As the process depends on the electronic structure and the electron-nuclear dynamics of the system, computational methods are well-suited to systematically investigate a plasmonic system of interest.

Theoretical investigations can offer detailed insight into the catalysis process. These methods can access important quantities like the electronic structure of the equilibrium system, the electron dynamics of the system upon excitation, and depending on the methods employed, coupled electron-nuclear dynamics to model activation and dissociation firsthand. However, modeling plasmonic photocatalysis is computationally demanding by nature, and becomes increasingly demanding as the size of the system or fidelity of the model is increased. The challenges involved in the theoretical modeling of plasmon-mediated photocatalysis range from technical issues like the accuracy vs. computational cost of a given method and its various approximations, to which information is relevant to extract from a given method, and even to the method-type itself.

Theoretical studies can be broadly divided into two camps: those that use potential energy surfaces (PES) to understand the system and its dynamics, and those that use a given "real-time" approach. In real-time approaches, typically the density matrix of the system is propagated in time upon perturbation by laser of a particular frequency and envelope, often without accessibility to distinct underlying potential energy surfaces (i.e. an Ehrenfest dynamics-type approach). In the PES approach, the topography of excited state surfaces is investigated. Sometimes, dynamics calculations are performed on these surfaces (e.g. surface hopping-type approaches) to provide transition probabilities between surfaces.[33]

In real-time approaches, there are several common approximations. Chief among them is in the choice of system model. Some studies have employed a jellium model for the nanoparticle portion of the system, such as in the work by Schatz and coworkers. This study found dissociation of the H_2 adsorbate on the jellium system at high field strengths.[34] Others, like our previous work[35] and that of Yan, et al.,[36] rely on small clusters that share key properties with more realistically sized nanoclusters in order to retain computational tractability. Others may examine realistically sized nanocluster-adsorbate systems with local density or generalized gradient-based functionals.[37] In these cases, similar to the jellium case, dissociation is achieved upon excitation at the quantum plasmon mode at a high electric field strength. Others still compute transition probabilities within the framework of electron-only dynamics rather than with explicit surfaces, which provides valuable information on electron-hole pairs and their probabilities of formation.[38,39] In all of these cases, density functional theory (DFT) is employed, which is less detailed than correlated wavefunction methods. Correlated wavefunction methods, while less common due to their computational cost, have been utilized in the unit cell-based embedding method PES-approach by Carter and coworkers, where the authors treat a portion of the system with a correlated wavefunction method and the remainder of the system with DFT in order to obtain excited state potential energy surfaces of the surface-adsorbate system.[40] However, in general, DFT is the workhorse method in the field.

Herein, we employ a model system of an atomic Ag_8 wire that retains key properties of larger wires. In particular, the system is too small to support a traditional plasmon mode, and instead exhibits longitudinal and transverse "quantum plasmon" modes. While the plasmon mode of large nanoparticles can be described through the classical Mie theory,[3] this picture breaks down for small clusters, where the states involved are sufficiently discretized. However, the picture of

"sloshing electron density" remains. In this case, the plasmon excitation can be described as a constructive addition of multiple single-particle transitions (or excited determinants). The multideterminantal excitations in silver and gold nanoparticles are collective in nature and grow to match the plasmon peaks as the particle size increases. As the particle size decreases, fewer determinants contribute to the plasmon. For the atomic scale nanowires, the transverse peak is still collective. However, the longitudinal peak becomes a single-particle transition at this size. Nonetheless, one can think of this as the limiting case as N → 1, where N is the number of determinants that comprises the plasmon-like excitation. The longitudinal peak in atomic scale wires still arises from delocalized sp → sp transitions with similar physics to the collective plasmons of larger nanorods. Thus, although this peak has 'single-particle' character, it is analogous in many ways to the 'plasmonic' transitions of larger systems. We refer the reader to more extensive discussions on this topic by Guidez and Aikens,[31,32] and Gieseking.[41,42] Studying a quantum plasmon excitation has several advantages, mainly in that it allows us to develop an understanding of plasmon-mediated photocatalysis through the lens of quantum chemistry rather than through a classical electrodynamics approach. That the quantum plasmon descriptor is especially appropriate for small, computationally tractable clusters, is appealing as well.

In this work, we build on a previous report in which we evaluated the electronic structure and dynamics of a system of N_2 on Ag_n (n = 6, 8, 10) wires.[35] We expand this initial report to study both N_2 and H_2 as the adsorbate molecule, to study the adsorbate in multiple orientations, and to study both the longitudinal and transverse quantum plasmon excitations of the Ag_8 wire. We find that in each adsorbate case the longitudinal plasmon mode leads to greater activation and/or dissociation for a given adsorbate configuration.

2. Methods

In all calculations, we employ the LC-ωPBE functional[43] and lanl2dz basis set,[44–46] as this functional/basis set combination has been found to perform well in our own benchmarking on the Ag_6N_2 system, and the LC-ωPBE functional is known to perform well for silver clusters.[47–50] The Ag_8N_2 and Ag_8H_2 structures were optimized in Gaussian 16[51] by first separately finding the geometry minima of the wire and small molecule, then combining the optimized structures to obtain Ag_8X_2 (X = N, H). The Ag_8X_2 structure is then optimized with the Ag atoms frozen, allowing the small molecule to orient about the wire while maintaining the linear symmetry of the

wire. We apply this procedure to four cases: Ag_8N_2 and Ag_8H_2 each in the parallel orientation (figure 1a) and the perpendicular orientation (figure 1b). For the Ag_8H_2 case, the parallel Ag-H distance is 2.53 Å, as is the distance to the center of the H_2 in the perpendicular case. In both Ag_8H_2 cases, the H_2 interatomic distance is found to be 0.75 Å.

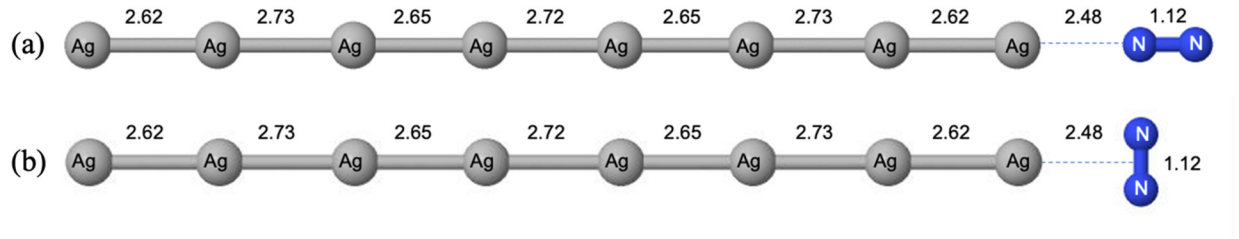


Figure 1. Ag_8N_2 structures. (a) "parallel" N_2 geometry, (b) "perpendicular" N_2 geometry. In the parallel case, we define N1 (H1) as the adsorbate atom closest to the wire, and N2 (H2) the terminal adsorbate atom. In the perpendicular case, N1 (H1) is defined as the atom above the longitudinal axis, and N2 (H2) the atom below.

We employ linear response time-dependent density functional theory (LR-TDDFT) to compute simulated absorption spectra using the standard implementation of the Gaussian 16 package. LR-TDDFT describes a given excitation in terms of linear combinations of single-particle transitions. Thus, in the molecular orbital picture, it provides information on which occupied-to-virtual orbital transitions comprise an excitation. In LR-TDDFT, a stick spectrum is obtained directly from the excitation energies and oscillator strengths of the excitations. In the absorption spectra presented herein, we convolve the stick spectrum with a Lorentzian broadening function with a full width at half-maximum (FWHM) of 0.2 eV. Absorption spectra intensities are shown in arbitrary units.

Electron-only real-time time-dependent density functional theory (RT-TDDFT) provides dynamical information on a system by obtaining its electronic response to an electric field perturbation. Unlike LR-TDDFT, RT-TDDFT is not limited to the perturbative regime, and the electronic response can be non-linear. RT-TDDFT provides access to the time-dependent dipole moment and other time-dependent quantities like time-dependent orbital populations (by projecting electron densities onto the ground-state orbitals).[52] We use a development version of Gaussian 16 for our RT-TDDFT calculations.[53] We apply a continuous-wave electric field at

electric field strengths of 0.001, 0.01, 0.03, and 0.05 atomic units (a.u.) at a given excitation energy of interest, which are the transverse and longitudinal plasmon excitations of the system. The electric field has a trapezoidal envelope, which is ramped to maximum intensity from 0-1 fs, then sustained at this intensity for 18 fs, before ramping down in the final 1 fs, for a total of 20 fs of "on" electric field. The equation for this field is shown in equations 1 and 2, where *t* is measured in fs:

$$E(t) = A(t)\sin(\omega t) \quad \text{(Eq. 1)}$$

$$A(t) = \begin{cases} E_0 t, & 0 < t < 1 \\ E_0, & 1 \leq t \leq 19 \\ -E_0(t-20), & 19 < t < 20 \end{cases} \quad \text{(Eq. 2)}$$

where E_0 represents the maximum electric field strength and ω is the frequency that corresponds to the excitation energy of interest.

We use an electronic step size of 0.0006 fs for the Ag_8N_2 cases. Each simulation is run for a minimum of 70 fs. In these electron-only calculations, we report only the first 20 fs of the 70 fs, since these calculations are used to compare against the results of the coupled Ehrenfest dynamics calculations, and as the adsorbate moves further away from the wire in the Ehrenfest dynamics calculations, comparison with RT-TDDFT results becomes increasingly tenuous.

Electron-only RT-TDDFT can be coupled with the mean-field Ehrenfest dynamics (ED) method to incorporate nuclear motion into a simulation, which we denote here as RT-TDDFT/ED. RT-TDDFT/ED allows for nuclear motion as described under the Ehrenfest scheme, where the nuclei are propagated based on the average forces from the electronic degrees of freedom at a given time step. Under this scheme, we can observe activation and dissociation of the N_2 or H_2 bond under a given excitation. As in the RT-TDDFT case, we use a development version of Gaussian 16 for our RT-TDDFT/ED calculations. Again, we apply the 20 fs trapezoidal-envelope continuous wave electric field. We use an electronic step size of 0.00025 fs and a nuclear step size of 0.1 fs for a minimum of 70 fs with default initial velocities on the adsorbate atoms. The Ag atoms are frozen. Field strengths of 0.05, 0.04, 0.03, 0.02, 0.01, and 0.001 a.u. are used. These electric field strengths are far outside the perturbative regime. As noted in works employing similar methodologies by Schatz and coworkers[34] and Meng and coworkers,[37] due to the high computational cost of dynamical quantum mechanics methods like Ehrenfest dynamics, dissociation or activation dynamics must be observed within the relatively short time window of

the simulation in order to maintain computational feasibility, which necessitates a strong electric field strength. Second, the duration of the applied electric field (20 fs in this work) is short compared to experimental irradiation times (~ 1 s), which leads to less energy transfer. Ongoing work in our group has explored the electric field relationship to the length of the silver atomic wires, finding that as the size of the particle increases, the applied electric field strength can decrease. We excite the system at the energies corresponding to the transverse and longitudinal plasmon excitations.

3. Results and Discussion

a. Parallel Ag_8N_2 at 0.03 a.u. electric field strength

In order to detail the computation and analysis process, we first walk through our approach with an example calculation, which is the response of the Ag_8N_2 system to a 0.03 a.u. continuous-wave electric field. In this case, our Ehrenfest dynamics results show activation of the N_2 bond, but not dissociation. First, to determine the appropriate energy at which to excite the system, both for the 0.03 a.u. electric field and for any other electric field for a given wire-small molecule orientation, we perform an LR-TDDFT calculation to identify interesting excitations of the system and their corresponding energies. The LR-TDDFT results (figure 2a) tell us the excitation energies and which single-particle transitions comprise each stick excitation. In this section we focus on the peak at 1.47 eV, which is comprised of two single-particle transitions, a HOMO → LUMO and HOMO – 1 → LUMO + 1. The orbitals are shown in (b).

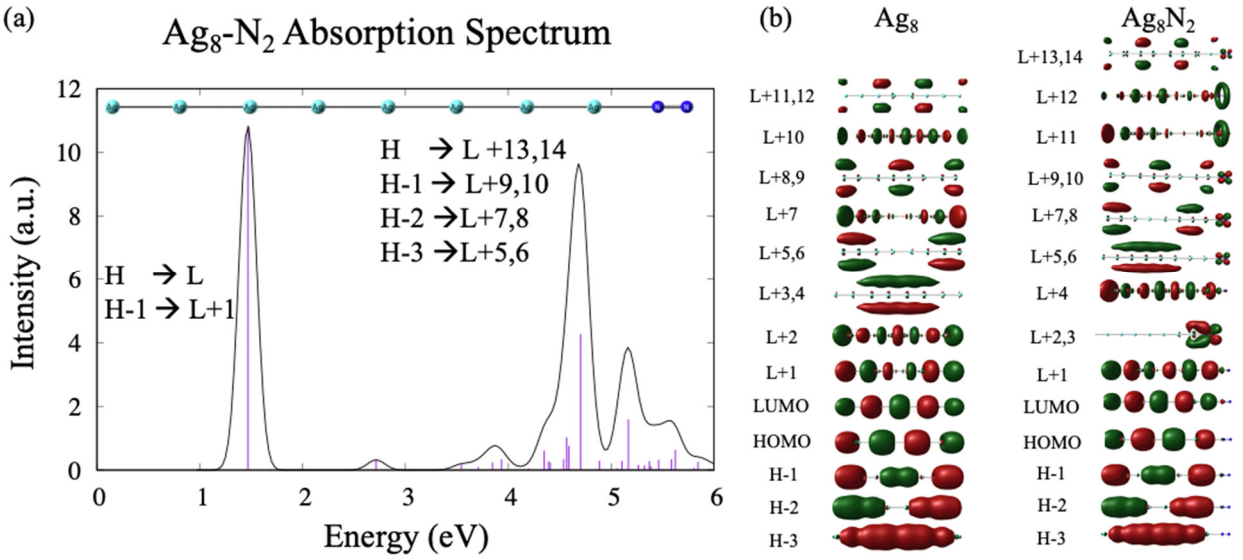


Figure 2. (a) LR-TDDFT absorption spectrum of parallel-oriented Ag_8N_2. The quantum plasmon peaks are labeled, and the corresponding single-particle transitions are shown, where "H" denotes HOMO and "L" denotes LUMO. In the LR-TDDFT spectrum, a.u. denotes "arbitrary units". (b) The orbitals in the range of relevant single-particle transitions for the longitudinal and transverse plasmon modes shown in (a). Figure adapted from reference 35.[35]

After identifying the peak of interest, we can perform an Ehrenfest dynamics calculation in which we excite this state of interest. We excite the system by driving the continuous wave electric field at the energy of the longitudinal plasmon-like mode identified via LR-TDDFT for 20 fs, then let the system propagate field-free for another 50 fs. From the Ehrenfest dynamics calculation, we can extract the nuclear coordinates at each time step, and from this information generate plots of bond distances over time and, if the bond distance over time oscillates due to nuclear vibrations rather than dissociates, compute a Fourier transform of the bond distance data to yield the frequency of the vibration.

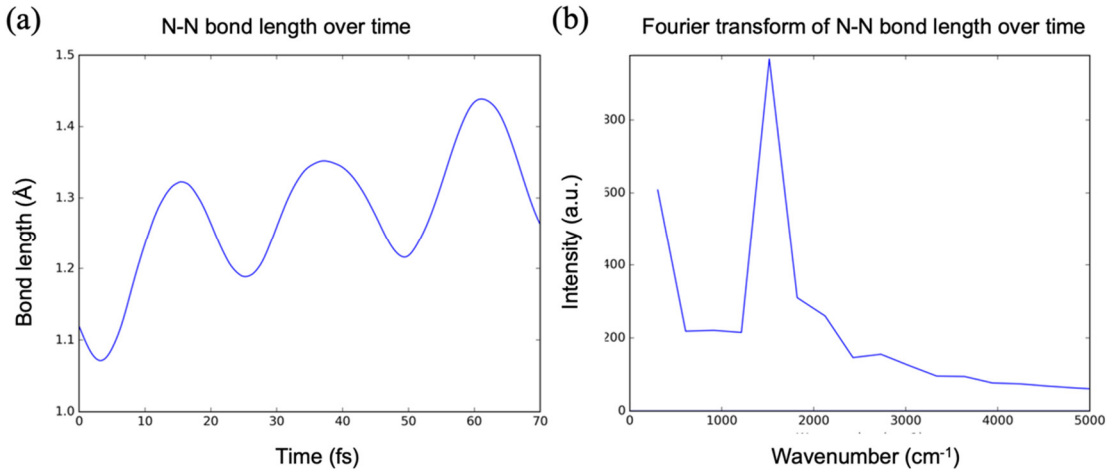


Figure 3. (a) N-N bond length across 70 fs RT-TDDFT/ED calculations in which a 0.03 a.u. electric field is applied, exciting at the longitudinal plasmon resonance energy. Plots for all possible electric field and N_2 orientations are shown in figure S1. (b) Fourier transform of the data shown in (a), which provides information about the vibrational frequency of the N-N bond across the simulation. The intensity is shown in arbitrary units.

The 0.03 a.u. electric field causes the N_2 molecule to vibrate around an average bond distance of 1.31 Å at a frequency of 1500 cm^{-1}, and we see that the average bond length continues to grow across the simulation, even after the electric field is turned off. The N_2 vibrational mode of Ag_8N_2 identified by Hessian normal mode analysis is 2408 cm^{-1} (the isolated N_2 bond frequency computed by Hessian normal mode analysis is 2382 cm^{-1}) and the optimized bond distance of N_2 in the equilibrium Ag_8N_2 system is 1.12 Å, which shows that excitation at the longitudinal plasmon resonance of the wire increases the average bond length of N_2 and decreases its vibrational frequency, indicating activation of the bond. When the isolated N_2 molecule is subject to identical conditions (i.e. the same applied electric field) and identical analysis, we find an N-N average bond distance of 1.19 Å vibrating at a frequency of 2050 cm^{-1}. Thus, the presence of the wire is an important ingredient in the activation of the N_2.

Another quantity of interest obtained from a real-time calculation is the time-dependent dipole moment. As the time-dependent dipole moment is calculated as a charge times a distance, it provides insight into the amount of electron density displacement across the system as a function of time. The static dipole moment of the system is quite large, at 4.82 D (parallel) and 3.00 D (perpendicular). This can be explained by the fact that, while Ag_8 and N_2 are both separately relatively nonpolar systems, combining the two results in a separation of charge. With the dipole arising from charge across a distance, and the length of the system being considerable at 22.3 Å (parallel) and 22.0 Å (perpendicular), the static dipole moment is larger than one might expect upon combination of two non-polar systems.

Over the time period of the simulations, the N_2 molecule moves away from the wire and, in dissociative cases, the N atoms move away from each other. Because of this, the time-dependent dipole moment of an RT-TDDFT/ED calculation is difficult to interpret. Instead, we examine the time-dependent dipole moment results of the corresponding electron-only RT-TDDFT calculation, where all nuclei are frozen in place. For electron-only quantities, we present only the first 20 fs of the 70 fs simulation and note that the most interesting dynamics occur within the first 5 fs.

In the first five femtoseconds of the electron-only dynamics, we see a surge in the z-directional (longitudinal) dipole moment, signifying a large amount of electron density displacement from one end of the wire to the other. When the system is excited at a perturbative electric field strength, the dipole tends to follow the electric field (Figure S2) At non-perturbative

field strengths, such as at 0.03 a.u., self-interaction of the dipole moment causes interference, disrupting its ability to track with the electric field (Figure 4).

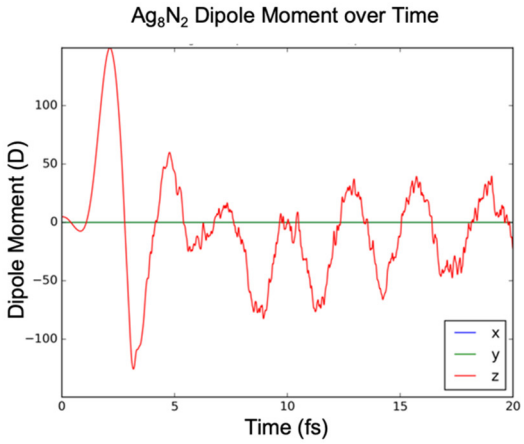


Figure 4. Time-dependent dipole for the first 20 fs of the electron-only RT-TDDFT calculation in which the longitudinal plasmon mode is excited with a 0.03 a.u. electric field. Note that the x- and y- directional dipoles overlay each other, as dipole moment experiences no change in either of these directions.

In addition to the time-dependent dipole moment, time-dependent orbital populations can be obtained as part of an RT-TDDFT calculation. Here, the electron density is projected onto the ground-state orbitals of the system at each time step. Since this analysis relies on the electronic structure at equilibrium geometry, time dependent orbital populations are only available in an electron-only dynamics calculation. In the first 20 fs of the electron-only simulation, the populations of the LUMO, LUMO+1, LUMO+4, and LUMO+11 rapidly increase on initial application of the electric field, with the LUMO spiking to a population of 0.97 at t = 1.96 fs. The LUMO+1, LUMO+4, and LUMO+11 have the same symmetry as the LUMO (i.e. Σ-symmetry, or cylindrical symmetry about the longitudinal axis). In the LR-TDDFT absorption spectrum, the longitudinal plasmon peak is comprised of the HOMO → LUMO and HOMO – 1 → LUMO + 1 transitions. Here, we see the involvement of additional transitions between orbitals with matching Σ-symmetry due to the non-perturbative nature of the applied electric field. In conjunction with the population of the LUMO, LUMO+1, LUMO+4, and LUMO+11 orbitals rapidly increasing, the population in HOMO, HOMO-1, HOMO-2, and HOMO-3 rapidly decreases.

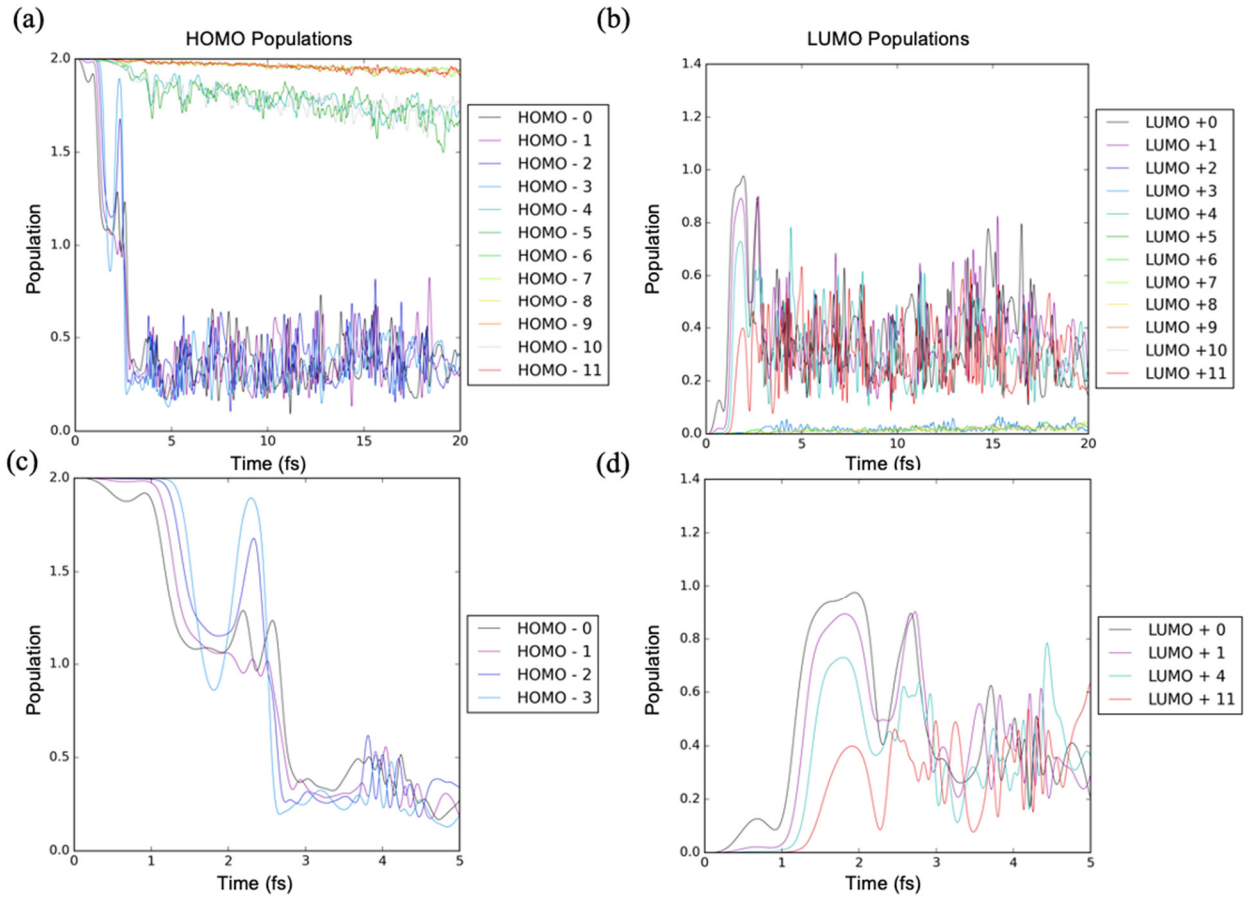


Figure 5. Time-dependent orbital populations for the 0.03 a.u. electric field, longitudinally excited parallel Ag_8N_2 system electron-only RT-TDDFT calculation. (a) Depicts population of initially occupied molecular orbitals, while (b) depicts the population of initially unoccupied orbitals. HOMO and LUMO populations for all simulations are shown in Figures S3-S6. (c) and (d) show the first 5 fs of orbital populations of the most affected occupied and unoccupied molecular orbitals respectively.

Finally, we carry out Hirshfeld population analysis at each time step on both the RT-TDDFT/ED calculation and the electron-only calculation. In this section, we present the ED results for the 0.03 a.u. electric field, parallel N_2 orientation, and longitudinal excitation system, though the full Hirshfeld population results for all Ag_8N_2 systems can be found in figures S7-S8, and the electron-only results can be found in figures S9-S10. We briefly discuss some of the differences between the RT-TDDFT and RT-TDDFT/ED results in section 3b. Atomic populations are not experimental observables, and because of this, there are multiple schemes to partition partial charges amongst atoms. We choose Hirshfeld population analysis in order to avoid the basis set

dependence of Mulliken-type methods.[54] Since the Hirshfeld method is density-based and relies on atomic reference densities, it is a better candidate for the RT-TDDFT/ED cases, where the electron density is propagated in time and atoms may migrate away from each other. Figure 6a partitions the Hirshfeld charges into N and Ag; the green line is the sum of the charge on both N atoms, while the blue line is the sum of all charge on each of the eight Ag atoms. The negative charge transfer to the adsorbate peaks at a charge of q = -0.935 at t = 15.3 fs. Figure 6b further partitions the adsorbate subsystem into atoms N1 and N2, where N1 is the nitrogen atom closest to the wire at the start of the simulation. The terminal N2 initially picks up more negative charge than N1. This charge transfer profile provides support for the idea that transient negative ions play an important role in plasmon-mediated molecular activations.[55] For this system (parallel adsorbate, longitudinal plasmon excitation, 0.03 a.u. field strength), a transient negative ion forms within the first 5 fs of the simulation, then dissipates around 42 fs into the simulation. This charge then oscillates between the two N atoms and the Ag wire. The maximum charge difference between the two nitrogen atoms, defined as $|q_{N1}-q_{N2}|$, is found to be 0.66, occurring 11.7 fs into the simulation.

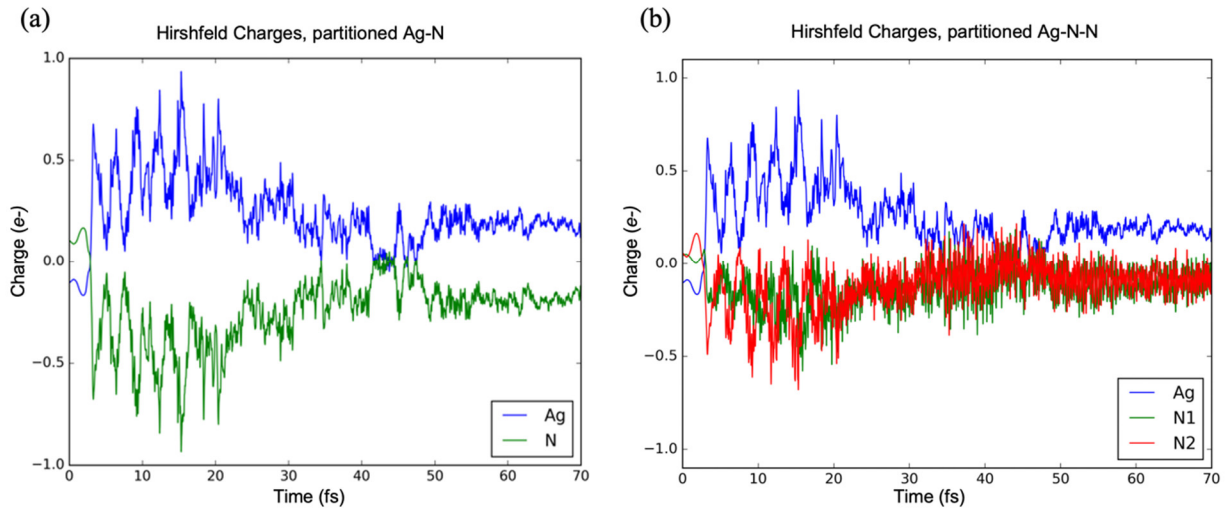


Figure 6. Time-dependent Hirshfeld charges. In (a), the charges are divided into Ag and N subsystems, where the Ag subsystem is the sum of all charges on each of the eight Ag atoms, and the N subsystem is the sum of the charges on the two N atoms. In (b), the Ag subsystem remains the same, but the charges on the two N atoms are plotted separately. N1 denotes the N atom closest to the wire at the start of the simulation, and N2 denotes the terminal N atom.

The Hirshfeld charge data, bond length data, and frequency analysis obtained from the RT-TDDFT/ED simulation, alongside electron-only dynamics to obtain orbital populations and dipole moment, provide insight into the charge transfer process that enables activation of the adsorbate. RT-TDDFT/ED data shows an overall increasing bond length with simulation time and a dominant N_2 vibrational frequency of about 1500 cm^{-1}. The average N_2 bond length in the 0.03 a.u. electric field is 1.31 Å, or 117% of the equilibrium length. The maximum bond length achieved is 1.44 Å, or 128% the equilibrium bond length, demonstrating activation of N_2. Meanwhile, the electron-only dipole moment shows a surge upon initial application of the field, signifying a large displacement of the electron density across the length of the wire. Simultaneously, the population of Σ-symmetry unoccupied orbitals rapidly grows as the population of the HOMO to HOMO-3 depletes in the first 5 fs. Finally, Hirshfeld charge analysis of the electron-nuclear dynamics calculation shows charge transfer occurs from the wire subsystem to the adsorbate, peaking at a charge of -0.935 *e*- at 15.3 fs.

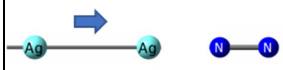
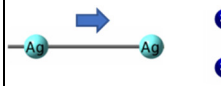
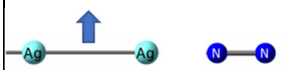
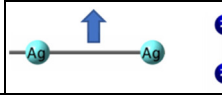
b. Ag_8N_2 Electron- and Electron-Nuclear Dynamics

While the above discussion presents a detailed analysis for a representative adsorbate orientation, excitation energy, and electric field strength, in this section, we focus primarily on comparing the time-dependent N-N bond distance and maximum charge on the N_2 in a series of RT-TDDFT/ED calculations. The systems examined are the possible combinations of the "parallel" (with longitudinal and transverse plasmon peaks at 1.47 eV and 4.68 eV, respectively) and "perpendicular" geometries (with longitudinal and transverse plasmon peaks at 1.46 eV and 4.64 eV, respectively) (figure 2a), continuous-wave excitation at the longitudinal and transverse plasmon mode energies, and electric field strengths of 0.05, 0.04, 0.03, 0.02, 0.01, and 0.001 a.u. for a total of 24 different Ag_8N_2 RT-TDDFT/ED simulations (Figure S1). From the N-N bond distance over time, we compute the N-N vibrational frequency via Fourier transform. We note that, due to the length of the calculations and consequently the relatively small number of oscillation cycles, the Fourier transform data is broad and contains a high amount of uncertainty. Despite this, general trends in the vibrational frequencies can be observed.

From Table 1 we observe that excitation of the longitudinal plasmon resonance leads to the most activation at a given field strength. Activation is most favorable in the "parallel" orientation, where dissociation is observed for the 0.05 a.u. field case. In the "perpendicular" orientation, the

N_2 also becomes activated, but to a generally lesser degree (or the same degree, in the 0.01 and 0.001 a.u. field cases). Some activation is observed for excitation of the transverse plasmon as well (4.68 eV), but not to the extent of the longitudinal plasmon case (1.47 eV), which may be due to the increased oscillator strength of the longitudinal plasmon relative to the transverse. Importantly, without the wire present, no activation of N_2 is observed, despite the significant strength of the applied electric field.

Table 1. Average N-N interatomic distance across 70 fs of RT-TDDFT/ED simulation. The truncated systems shown in the "adsorbate orientation and electric field polarization" cells represent the four possible orientation/electric field combinations. Respectively, these are parallel-oriented adsorbate excited at the longitudinal plasmon mode, perpendicular-oriented adsorbate excited at the longitudinal plasmon mode, parallel-oriented adsorbate excited at the transverse plasmon mode, and perpendicular-oriented adsorbate excited at the transverse plasmon mode. Corresponding bond length plots are found in figure S1.

	Field strength (a.u.)	0.05	0.04	0.03	0.02	0.01	0.001
Adsorbate orientation and electric field polarization		2.47 Å	1.41 Å	1.30 Å	1.21 Å	1.16 Å	1.13 Å
		1.33 Å	1.27 Å	1.23 Å	1.18 Å	1.16 Å	1.13 Å
		1.17 Å	1.16 Å	1.16 Å	1.14 Å	1.14 Å	1.13 Å
		1.18 Å	1.18 Å	1.17 Å	1.15 Å	1.14 Å	1.13 Å

The table of N-N average vibrational frequencies (Table 2) provides insight into the degree of activation for the cases that do not fully dissociate. In the N_2 case, this is for all but one simulation. For comparison, the isolated N_2 stretching mode computed via Hessian normal mode calculation is 2383 cm^{-1}, whereas the N_2 stretching mode of Ag_8N_2 is 2408 cm^{-1}. In general, the vibrational frequency decreases as the electric field increases, which is consistent with the notion that as a bond becomes more activated, it becomes weaker and its vibrational frequency decreases. The lowest N_2 vibrational frequencies are achieved for high field strengths that are longitudinally polarized, with N_2 in the parallel orientation becoming particularly activated. Further, for the cases

in which the N_2 does not dissociate, the downward trend in the N_2 vibrational frequency generally tracks with the upward trend in bond length as the field strength increases. Note that excitation of the transverse plasmon mode does not strongly affect the N_2 vibrational frequency when N_2 is in either of the parallel or perpendicular orientations.

Table 2. N_2 vibrational frequency (cm^{-1}) across 70 fs RT-TDDFT/ED simulations for the systems described in Table 1.

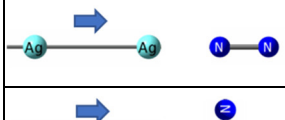
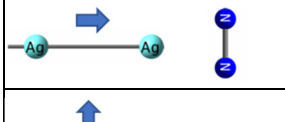
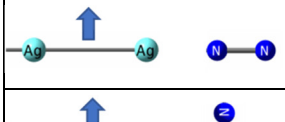
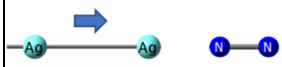
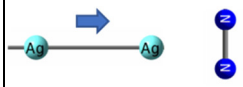
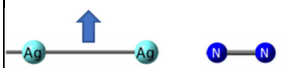
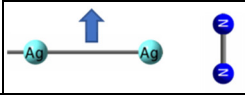
	field strength (a.u.)	0.05	0.04	0.03	0.02	0.01	0.001
Adsorbate orientation and electric field polarization		-	1200	1500	1700	2100	2300
		1100	1700	1500	2100	2200	2300
		2100	2000	2000	2100	2300	2200
		1900	2000	1900	2000	2200	2200

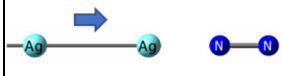
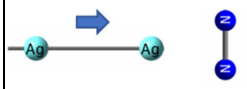
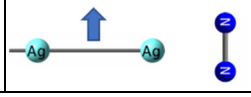
Table 3 compiles the maximum Hirshfeld charge obtained on the N_2 molecule across each simulation. Full Hirshfeld charge data plots are shown in Figure S7. Data for the timestep at which the maximum charge occurs is available in table S1. In general, calculations with stronger field strengths yield a more negative maximum charge, and this peak charge tends to occur earlier in the simulation. For a given electric field strength, the longitudinally polarized field with parallel-oriented N_2 sees the most charge transfer from the wire to the N_2, with the amount of charge transferred increasing as the field strength increases. The transverse-polarized electric field cases see little charge transfer in comparison to the longitudinally-polarized cases at a given field strength. The longitudinal field with perpendicular N_2 case sees considerably more charge transfer than the transverse field cases, but less than when the N_2 is oriented parallel to the wire. These results are consistent with the degree of activation (Table 1) and the change in N_2 vibrational frequency (Table 2). Cases in which more charge is transferred correlate with higher average N-N bond lengths and lower vibrational frequencies. In the transverse field case, little bond activation is seen, along with little charge transfer.

Table 3. Maximum Hirshfeld charge (e^-) obtained on N_2 subsystem across 70 fs of RT-TDDFT/ED simulation. The time at which the maximum charge is obtained is found in Table S1.

	field strength (a.u.)	0.05	0.04	0.03	0.02	0.01	0.001
Adsorbate orientation and electric field polarization		-1.06	-0.94	-0.94	-0.77	-0.44	-0.21
		-0.82	-0.73	-0.86	-0.65	-0.47	-0.21
		-0.42	-0.39	-0.32	-0.26	-0.25	-0.10
		-0.29	-0.37	-0.28	-0.25	-0.16	-0.09

In addition to the maximum Hirshfeld charge, we compute the maximum charge difference between N1 and N2 in each simulation, summarized in Table 4. Data on when the maximum charge difference occurs is available in Table S2, and the full Ag-N-N-partitioned Hirshfeld charge data is found in Figure S8. The trend in data for maximum $|q_{N1} - q_{N2}|$ generally follows the same trend as the maximum Hirshfeld charge, where the parallel-oriented N_2 at longitudinal plasmon excitation obtains the maximum charge separation for a given field strength, with perpendicularly-oriented N_2 at longitudinal plasmon mode obtaining smaller but still significant charge separations. Each transverse excitation case sees little charge separation, irrespective of field strength or N_2 orientation. It is possible that the greater degree of charge separation across parallel-oriented N_2 in the longitudinal case encourages the greater degree of activation relative to the perpendicular case. We hypothesize that the polarization of the bond may help facilitate the bond breakage.

Table 4. Maximum Hirshfeld charge difference obtained as $|q_{N1} - q_{N2}|$ across 70 fs of RT-TDDFT/ED simulation. The time at which the maximum charge difference is obtained is found in Table S2.

	field strength (a.u.)	0.05	0.04	0.03	0.02	0.01	0.001
Adsorbate orientation and electric field polarization		1.10	0.84	0.66	0.41	0.25	0.08
		0.45	0.55	0.39	0.22	0.19	0.06
		0.29	0.20	0.22	0.18	0.11	0.03
		0.24	0.22	0.18	0.13	0.09	0.03

The results obtained from the RT-TDDFT/ED simulations suggest that the orientation of the molecule along the wire is important for activation, that the degree of activation scales with the strength of the electric field, and that excitation of the transverse plasmon mode activates the system significantly less than the longitudinal plasmon mode, regardless of adsorbate orientation or field strength.

We can examine equivalent electron-only RT-TDDFT calculations for each RT-TDDFT/ED case. Again, projecting the electron density at a given timestep onto the ground-state orbitals can provide qualitative insight into the electron dynamics of the system through orbital population analysis, alongside electron-only time-dependent dipole and charge data. The electron-only dynamics data is reported in figures S2-S6 and figures S9-S10.

As in the RT-TDDFT/ED case that includes both electron and nuclear dynamics, we find that that the incident electric field matters more than the orientation of the N_2. Population analysis (figures S3-S6) reveals that the orbitals involved in a given simulation are those that are expected based on symmetry considerations, i.e. $\Sigma \rightarrow \Sigma$ transitions for the field polarized to the longitudinal plasmon, and $\Sigma \rightarrow \Pi$ transitions for the transverse case. With the stronger electric fields, more orbitals are involved than those found in the LR-TDDFT absorption calculation. For example, in the LR-TDDFT longitudinal plasmon excitation with N_2 in the parallel orientation, we find that

the orbitals involved are the HOMO-1, HOMO, LUMO, and LUMO+1. In the longitudinal excitation electron-only dynamics, we find for field strengths of 0.01 a.u. or stronger that other unoccupied orbitals of Σ symmetry, the LUMO+4 and LUMO+11, become occupied in addition to the LUMO and LUMO+1, and that the HOMO-2 and HOMO-3, in addition to the HOMO-1 and HOMO, lose occupation. Given that LR-TDDFT is a perturbative method, and field strengths of 0.01 a.u. or greater are not in the perturbative regime, observing additional symmetry-allowed single-orbital transitions within a given excitation is reasonable. However, it is unclear how or whether these additional single-particle excitations play an important role in the adsorbate activation process, as the population data is not available in the case of the full RT-TDDFT/ED simulations.

Electron-only time-dependent dipole moment and Hirshfeld charge data is also available from the electron-only calculations (figures S9-S10). These quantities generally resemble their electron-nuclear counterparts at the start of the simulation, which is when the electron-only and electron-nuclear systems most closely resemble each other. Comparison of the electron-only Hirshfeld charge data with the electron-nuclear data in the first 20 fs reveals that nuclear motion plays a role in the charge transfer process (figures S9-S10). Whereas electron-only charge oscillations tend to rebound to neutral or near-neutral charge, the simulations with mixed electron/nuclear dynamics tend to maintain a charge separation, i.e. demonstrate less "charge rebounding." Thus, nuclear motion may aid in maintaining the initial charge separation.

c. Ag_8H_2 at 0.03 a.u. electric field strength

While the N_2 results show dissociation and/or activation as a function of electric field strength, the N_2 molecule itself has a relatively complicated electronic structure, and the interplay between the electronic structure and dynamics outcomes is complex. In an effort to simplify the molecular electronic structure aspect of the model, we investigate Ag_8H_2 systems. In the H_2 case, any dissociative route likely results in population of the H_2 σ* orbital (or orbitals with H_2 σ* character). Similar to Ag_8N_2, we first provide the LR-TDDFT results, the RT-TDDFT/ED and electron-only RT-TDDFT calculations, and their analyses, for the parallel-oriented H_2 excited at the longitudinal plasmon resonance with an electric field strength of 0.03 a.u. We first compute the LR-TDDFT absorption spectrum (Figure 7) and examine the single-particle transitions involved in the longitudinal and transverse plasmon peaks.

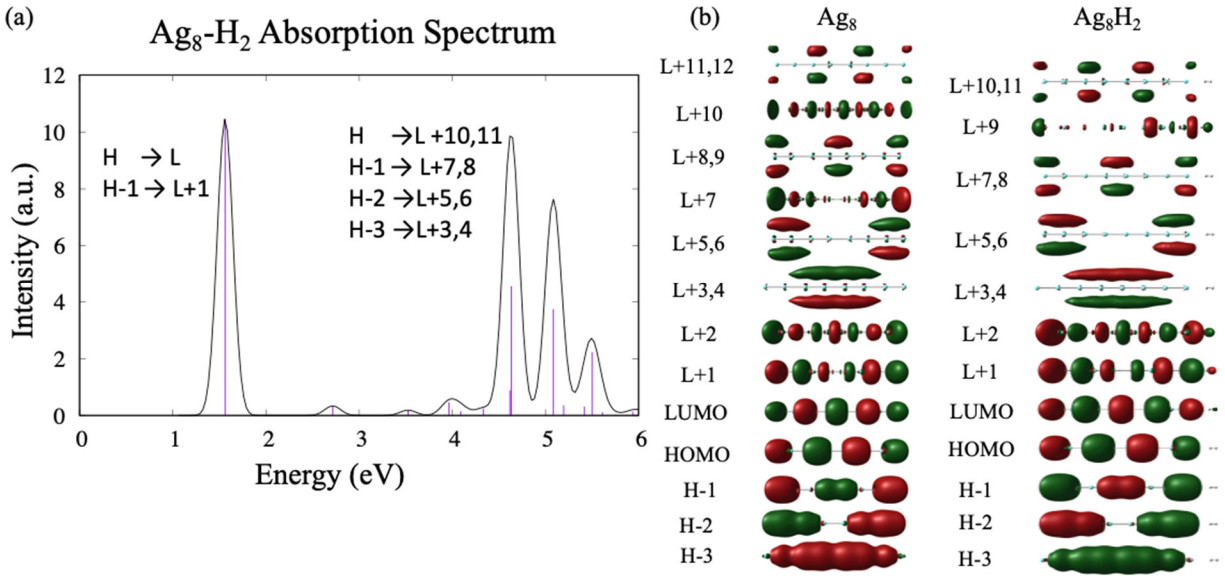


Figure 7. (a) LR-TDDFT absorption spectrum, with a.u. denoting arbitrary units. (b) The corresponding molecular orbitals of parallel-oriented Ag_8H_2.

Between Ag_8N_2 and Ag_8H_2, the symmetry of the transitions involved do not change for either the longitudinal or transverse modes, with the longitudinal mode comprised of $\Sigma_4 \rightarrow \Sigma_5$ and $\Sigma_3 \rightarrow \Sigma_6$ transitions (HOMO → LUMO and HOMO – 1 → LUMO + 1), and the transverse mode comprised of the $\Sigma_n \rightarrow \Pi_n$ transitions, where n = 1, 2, 3, 4. The energies of the two quantum plasmon peaks in Ag_8H_2 (Figure 7) are slightly shifted from the Ag_8N_2 case (Figure 2), with the longitudinal mode occurring at 1.44 eV and the transverse mode at 4.66 eV for the parallel oriented H_2 system (1.46 eV and 4.64 eV for the perpendicularly oriented H_2 case, respectively). Unlike the Ag_8N_2 case, the unoccupied Π orbitals contain no contribution from H_2-based atomic orbitals. That is, no hybridization of an H_2 π* orbital is found in the Π orbitals of the system, as expected. Meanwhile, the unoccupied Σ orbitals do retain H_2 σ* character.

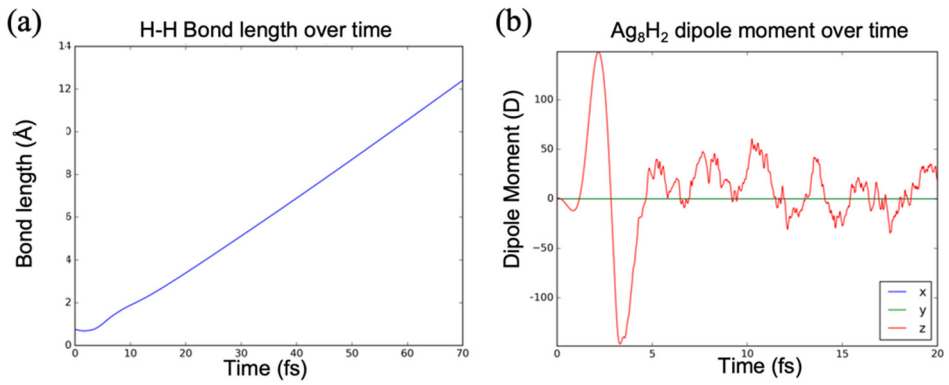


Figure 8. (a) H-H bond distance over 70 fs in the RT-TDDFT/ED simulation for parallel-oriented Ag_8H_2 excited at the longitudinal plasmon frequency with 0.03 a.u. electric field strength. Bond distances for all Ag_8H_2 cases are shown in Figure S11. (b) Time-dependent dipole corresponding to the equivalent electron-only RT-TDDFT calculation.

For the sake of comparison with the Ag_8N_2 case presented, we focus on the parallel-oriented adsorbate configuration. However, unlike Ag_8N_2, the orientation for Ag_8H_2 with H_2 perpendicular to the wire is lower in energy by -0.037 eV. On plotting the H-H bond distance over time, we see rapid dissociation occur soon after the onset of the electric field, with the two H atoms over 12 Å apart by 70 fs (Figure 8a). This is unlike the analogous Ag_8N_2 result, where the N_2 achieves a maximum of 0.32 Å bond elongation compared to the N_2 equilibrium bond, but ultimately does not dissociate within the simulation time frame (Figure 3). The accompanying Fourier transform for this Ag_8H_2 calculation is not shown, as the H_2 bond length does not demonstrate any oscillatory behavior throughout the course of the simulation. The time-dependent dipole moment (Figure 8b) appears similar to the analogous N_2 case (Figure 4) within the first 20 fs, especially in that a large electron density displacement is evident in the first few fs of the calculation. The time-dependent electron-only dipole moment is shown for all Ag_8H_2 cases in Figure S12.

Similar to the N_2 case, we partition the RT-TDDFT/ED Hirshfeld charges into Ag and H (figure 9a) and Ag, H1, H2 (figure 9b), where H1 is the H atom closest to the wire at the start of the simulation. The charge profile of the Ag_8N_2 system (Figure 6) appears significantly different than Ag_8H_2. In the Ag_8H_2 case, a large surge in charge separation occurs around 3 fs. The Ag_8 subsystem gains 1.2 *e*- positive charge as the H_2 subsystem gains 1.2 *e*- negative charge, where

the peak charge of -1.22 (units of *e*- used for all charges) is obtained at 3.4 fs. Thus, charge transfer occurs very soon after the start of the simulation, and at 5 fs, the H_2 bond length is 1.01 Å, or 135% of the equilibrium bond length. The equivalent Ag_8N_2 system does not obtain its maximum adsorbate charge until 15.3 fs, where it reaches -0.94 on the N_2. The Ag_8N_2 system achieves its maximum bond length of 1.44 Å at 61.6 fs, at which point the charge on N_2 is -0.25. In the first 10 fs of the calculations, the charge difference between H1 and H2 is much less than that of N1 and N2. However, in cases in which the H_2 activates but does not dissociate, the charge oscillations between H1 and H2 follow similar trends to that of the non-dissociated N1 and N2 (figures S13-S14). Despite very different methodology, we find that our H_2 charge transfer results are consistent with those found in Ref. 34, in that each finds the number of electrons increasing on the H_2 in the first 15 fs.

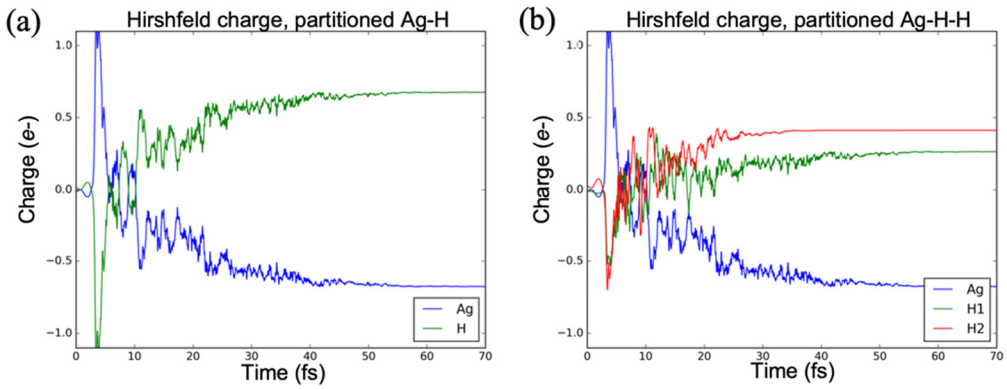


Figure 9. Hirshfeld charge over 70 fs of RT-TDDFT/ED simulation. (a) shows partitioning of charge into Ag and H subsystems. (b) plots the charge for each H atom separately.

The orbital populations can be extracted from the electron-only dynamics. We stress again that, soon after the start of the simulation, the electron-only dynamics will not mirror RT-TDDFT/ED results, especially in the case of a quickly dissociating adsorbate. Thus, we present only the first 20 fs of orbital populations, noting that, in this particular case, even by 20 fs, the H_2 in the Ehrenfest dynamics calculation has achieved an inter-hydrogen distance of 3.49 Å, over quadruple the equilibrium bond length. Similar to the Ag_8N_2 case, we see rapid initial population of the unoccupied Σ-geometry orbitals, and simultaneous depletion of the corresponding Σ occupied orbitals (Figure 10). Like Ag_8N_2 (Figure 5), we see more Σ-type orbitals involved than is

suggested by the LR-TDDFT calculation, which is due to the non-perturbative strength of the electric field.

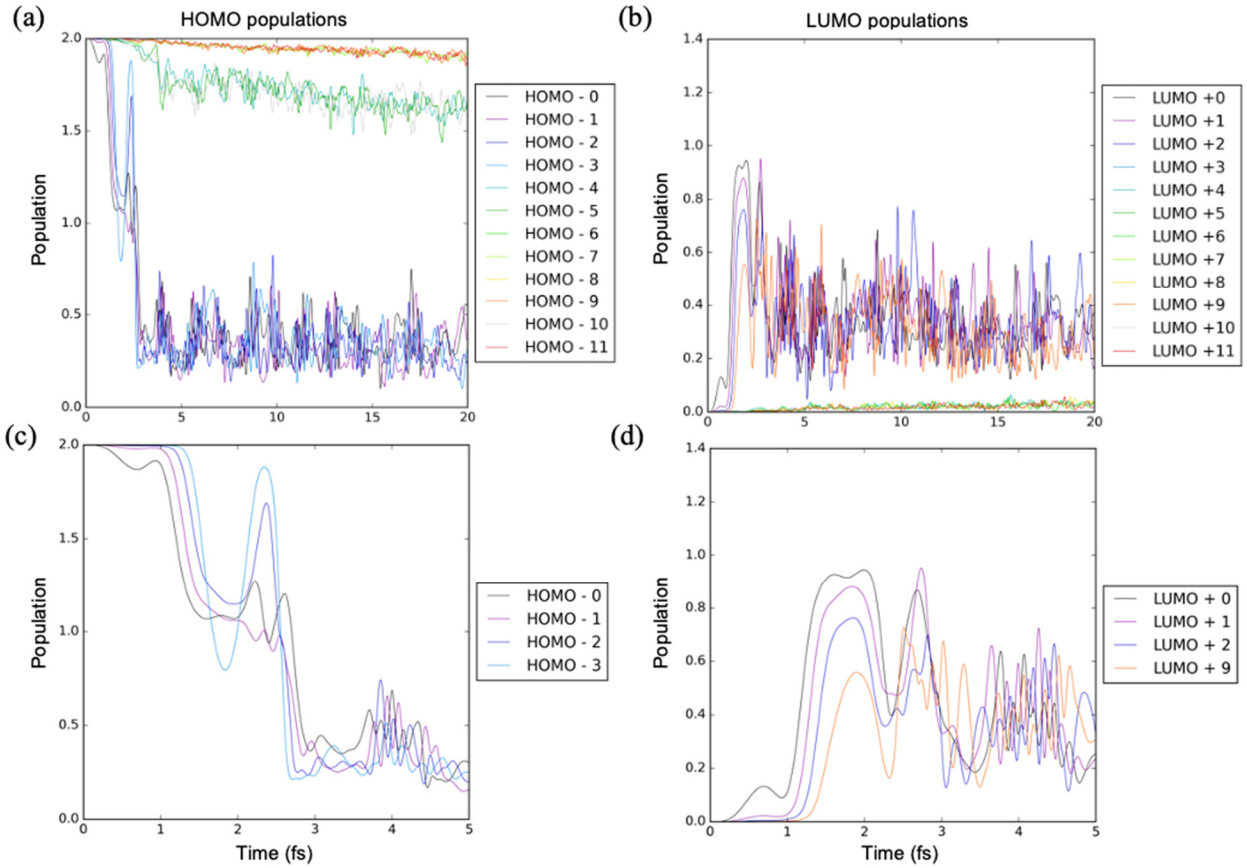


Figure 10. Time-dependent orbital populations for the corresponding 0.03 a.u. electric field, longitudinally excited Ag_8H_2 system electron-only RT-TDDFT calculation. (a) depicts population of initially occupied molecular orbitals, while (b) depicts the population of initially unoccupied orbitals. The HOMO and LUMO keys correspond to the orbitals in figure 7b. Plots for all simulations are located in figures S15-S18. (c) and (d) show the first 5 fs of orbital populations of the most affected occupied and unoccupied molecular orbitals respectively.

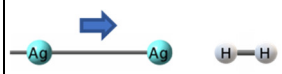
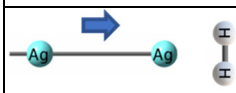
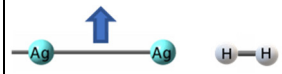
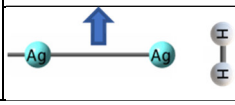
In general, the markers of activation are present in both the Ag_8N_2 and Ag_8H_2 cases. The electron-only orbital populations appear especially similar, even in the time at which population occurs and the degree of population. The sudden occupation of the Σ-type unoccupied orbitals, the large shift in dipole moment, and the charge transfer from the wire to the adsorbate are present in both the Ag_8N_2 and Ag_8H_2 cases. It is possible that H_2 dissociation occurs with the 0.03 a.u. applied

field whereas N_2 dissociation does not because H_2 is more weakly bound with a single σ bond, as opposed to the triple bond of N_2.

D. Ag_8H_2 Electron- and Electron-Nuclear Dynamics

Similar to the Ag_8N_2 case, we now focus on the average bond length and frequency data of the Ag_8H_2 RT-TDDFT/ED simulations, alongside the H_2 charge and $|q_{H1} - q_{H2}|$ charge difference data. Table 5 contains the average bond length of H_2 across the RT-TDDFT/ED simulations. In the H_2 case, the longitudinal plasmon excitation of the wire with parallel-oriented H_2 results in dissociation at the 0.03, 0.04, and 0.05 a.u. field strengths. The longitudinal plasmon excitation of the wire with perpendicularly oriented H_2 results in dissociation for the 0.05 a.u. electric field case. This contrasts with the analogous N_2 calculations, where only the parallel-longitudinal 0.05 a.u. case achieves full dissociation within 70 fs (Table 1). The trend of the longitudinal plasmon resonance activating significantly more than the transverse resonance holds for H_2 as well as N_2, as does the orientation trend that the parallel adsorbate typically activates more than the perpendicular adsorbate.

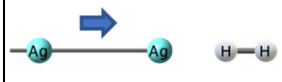
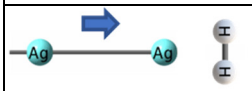
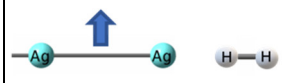
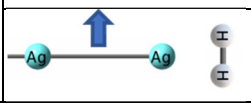
Table 5. Average H-H interatomic distance across 70 fs of RT-TDDFT/ED simulation. Corresponding plots are found in Figure S11.

	Field strength (a.u.)	0.05	0.04	0.03	0.02	0.01	0.001
Adsorbate orientation and electric field polarization		11.50 Å	7.89 Å	7.83 Å	0.81 Å	0.79 Å	0.76 Å
		4.00 Å	0.88 Å	0.83 Å	0.77 Å	0.90 Å	0.75 Å
		0.84 Å	0.83 Å	0.79 Å	0.78 Å	0.76 Å	0.76 Å
		0.85 Å	0.90 Å	0.77 Å	0.76 Å	0.75 Å	0.75 Å

H_2 vibrational activation (Table 6) sees similar trends to the N_2 vibrational activation (Table 2) in that, as the electric field increases, the H_2 vibrational frequency tends to decrease. In both the N_2 and H_2 case, with our data, it is impossible to ascertain whether or not the decreases in

vibrational frequency are due to excitement onto higher vibrational states (e.g. in the anharmonic well of the ground electronic state, which leads to lower vibrational frequencies as the vibrational energy level increases), or due to excitement onto higher electronic states, which tend to have shallower wells and will result in the same outcome. RT-TDDFT/ED calculations do not allow for analysis of either of these quantities. Thus, we can observe the decreasing frequency with increasing electric field and correlate this to the increase in adsorbate activation, but cannot assert whether this activation is vibrational or electronic in nature.

Table 6. H_2 vibrational frequency (cm^{-1}) across 70 fs RT-TDDFT/ED simulation.

	Field strength (a.u.)	0.05	0.04	0.03	0.0	0.01	0.001
Adsorbate orientation and electric field polarization		-	-	-	3600	3600	4100
		-	2900	4000	4100	3400	4000
		3300	3300	3700	4000	4400	4000
		3400	3100	3900	4100	4000	4100

The maximum charge obtained on the H_2 subsystem (Table 7) does not correlate as strongly to H_2 activation as the maximum charge on N_2 tracks with N_2 activation (Table 3). The maximum charge difference between the two H atoms also correlates less strongly with activation than the N_2 case. For each quantity, there is a general trend that for a given field strength, the parallel-longitudinal simulations gain the most charge and obtain the largest charge difference (Table 8), followed by perpendicular-longitudinal, then parallel-transverse, and finally perpendicular-transverse. This is consistent with the N_2 results. However, the trend in correlation between electric field strength and maximum adsorbate charge and maximum adsorbate charge difference is less clear in the H_2 case. While the Hirshfeld charge analysis reveals charge transfer occurring in both the N_2 and H_2 cases, H_2 tends to pick up a smaller maximum charge and maximum charge difference, while still activating more readily. This may be due in part to N_2's increased ability to house additional negative charge relative to H_2, given its more complex electronic structure and

availability of lower-lying unoccupied orbitals. N_2 may have more channels of activation and dissociation due to these lower lying orbitals, as well as its increased orbital hybridization into the wire relative to H_2. A comparison of electron-only and electron-nuclear Hirshfeld charges for the first 20 fs of simulation can be found in figures S19-S20. The difference in degree of "charge rebounding" as discussed for the Ag_8N_2 case in section 3c appears much less significant in the Ag_8H_2 case. The significant activation of H_2 within 20 fs in the RT-TDDFT/ED results (Figure S11) more severely limits comparison between the Hirshfeld charges of electron-nuclear and electron-only calculations.

Table 7. Maximum negative Hirshfeld charge obtained on the H_2 subsystem across 70 fs of RT-TDDFT/ED simulation. The time at which the maximum charge occurs is listed in Table S3.

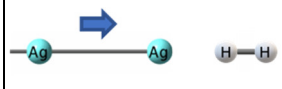
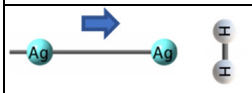
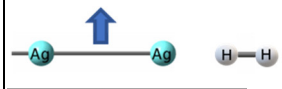
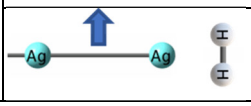
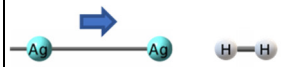
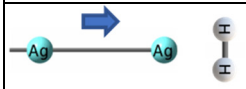
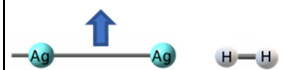
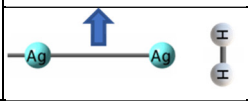
	field strength (a.u.)	0.05	0.04	0.03	0.02	0.01	0.001
Adsorbate orientation and electric field polarization		-0.86	-0.67	-1.22	-0.99	-0.61	-0.07
		-0.55	-0.50	-0.65	-0.60	-0.52	-0.08
		-0.32	-0.30	-0.17	-0.16	-0.05	0.00
		-0.24	-0.47	-0.19	-0.15	-0.05	0.00

Table 8. Maximum Hirshfeld charge difference obtained as $|q_{H1} - q_{H2}|$ across 70 fs of RT-TDDFT/ED simulation. The time at which the maximum charge difference occurs is listed in Table S4.

	field strength (a.u.)	0.05	0.04	0.03	0.02	0.01	0.001
Adsorbate orientation and electric field polarization		0.48	0.82	0.56	0.28	0.09	0.04
		0.40	0.33	0.32	0.15	0.19	0.04
		0.30	0.19	0.14	0.11	0.07	-
		0.20	0.24	0.10	0.10	0.06	-

Examining the average bond length for the parallel-longitudinal case side-by-side (Table 9), the H_2 case activates slightly more as a percent of the equilibrium bond length for a given field strength, and more cases result in full dissociation. These results, together, suggest that cleavage of the Σ bond is important in both cases, as the parallel orientation with excitation at the longitudinal resonance promotes symmetry-allowed access to the adsorbate Σ bonds, and the transverse mode, despite allowing easier access to excitation to the H_2 and N_2 σ* orbitals in their perpendicular orientations, is a weaker excitation than the longitudinal mode. Moreover, the transverse peak is comprised of degenerate x- and y- directional excitations, while the RT-TDDFT/ED calculations excite only one of the two directions, effectively halving the oscillator strength, which may explain why the transverse excitation only minimally activates the adsorbate. We have shown the percent-hybridization of the adsorbate atomic orbitals into the frontier molecular orbitals in tables S5 and S6.

Table 9. Comparison of average adsorbate bond length in Å across the first 70 fs of RT-TDDFT/ED simulation between Ag_8H_2 and Ag_8N_2. Parentheses denote the length as a percentage of the equilibrium bond length, shown in the rightmost column.

Field Strength (a.u.)	0.05	0.04	0.03	0.02	0.01	0.001	0.00
Ag_8H_2	11.50 (n/a)	7.89 (n/a)	7.83 (n/a)	0.81 (109%)	0.79 (107%)	0.76 (103%)	0.74
Ag_8N_2	2.47 (n/a)	1.41 (126%)	1.30 (116%)	1.21 (108%)	1.16 (103%)	1.13 (101%)	1.12

4. Conclusion

We have examined an array of real-time dynamics calculations of Ag atomic wire-adsorbate systems, analyzing both Ehrenfest dynamics and electron-only dynamics of these systems. We examine adsorbate orientations perpendicular and parallel to the wire, and we examine excitations at the longitudinal and transverse plasmon energies. The adsorbates examined are H_2 and N_2, where we find that H_2 generally activates or dissociates more readily than N_2 for the same electric field, adsorbate orientation, and excitation energy. For all cases, excitation at the longitudinal mode activates the adsorbate considerably more than the transverse mode. The degree of activation of adsorbate depends on the strength of the electric field, where electric field strengths of 0.05, 0.04, 0.03, 0.02, 0.01, and 0.001 a.u. are examined. Through Hirshfeld population analysis, we observe charge transfer from the wire to the adsorbate. In the N_2 case, the degree of charge transfer tracks generally with the strength of the electric field. The same trend does not hold for the H_2 case, which may be due to the more limited electronic structure of H_2, which has fewer channels in which to gain additional negative charge. In each case, we can observe the formation of an adsorbate transient negative ion. We postulate that adsorbate Σ bond cleavage is critical in both cases. In the H_2 case, this is the only dissociation channel. In the N_2 case, the dependence on the parallel orientation and the longitudinal excitation suggests that Σ bond cleavage plays a pivotal role. In the parallel case, we observe significant charge differences between the nitrogen atom closest to the atomic wire and the nitrogen atom further from the wire, which may aid in dissociation.

Supporting Information Available

Time-dependent bond lengths, dipole moments, frontier orbital populations, and Hirshfeld charges and charge differences during RT-TDDFT and RT-TDDFT/ED simulations of Ag_8N_2 and Ag_8H_2. Percent contributions of N_2 and H_2 atomic orbitals in Ag_8N_2 and Ag_8H_2 molecular orbitals.

Acknowledgments

We gratefully acknowledge David Lingerfelt and Xiaosong Li for the RT-TDDFT and RT-TDDFT/ED code. This material is based on work supported by the Department of Energy under grant DE-SC0012273. O.H. has been supported by the Department of Energy Computational Science Graduate Fellowship under grant number DE-SC0019323. The computing for this project was performed on the Beocat Research Cluster at Kansas State University, which is funded in part by NSF grants CHE-1726332, CNS-1006860, EPS-1006860, and EPS-0919443.

References

(1) Robatjazi, H.; Yuan, L.; Yuan, Y.; Halas, N. J. Heterogeneous Plasmonic Photocatalysis: Light-Driven Chemical Reactions Introduce a New Approach to Industrially-Relevant Chemistry. In *Emerging Trends in Chemical Applications of Lasers*; ACS Symposium Series; American Chemical Society, 2021; Vol. 1398, pp 363–387.

(2) Zhang, Z.; Zhang, C.; Zheng, H.; Xu, H. Plasmon-Driven Catalysis on Molecules and Nanomaterials. *Acc. Chem. Res.* **2019**, *52*, 2506–2515.

(3) Kelly, K. L.; Coronado, E.; Zhao, L. L.; Schatz, G. C. The Optical Properties of Metal Nanoparticles: The Influence of Size, Shape, and Dielectric Environment. *J. Phys. Chem. B* **2003**, *107*, 668–677.

(4) Gellé, A.; Jin, T.; de la Garza, L.; Price, G. D.; Besteiro, L. V.; Moores, A. Applications of Plasmon-Enhanced Nanocatalysis to Organic Transformations. *Chem. Rev.* **2020**, *120*, 986–1041.

(5) Christopher, P.; Linic, S. Engineering Selectivity in Heterogeneous Catalysis: Ag Nanowires as Selective Ethylene Epoxidation Catalysts. *J. Am. Chem. Soc.* **2008**, *130*, 11264–11265.

(6) Zhang, Y.; He, S.; Guo, W.; Hu, Y.; Huang, J.; Mulcahy, J. R.; Wei, W. D. Surface-Plasmon-Driven Hot Electron Photochemistry. *Chem. Rev.* **2018**, *118*, 2927–2954.

(7) Mukherjee, S.; Libisch, F.; Large, N.; Neumann, O.; Brown, L. V.; Cheng, J.; Lassiter, J. B.; Carter, E. A.; Nordlander, P.; Halas, N. J. Hot Electrons Do the Impossible: Plasmon-Induced Dissociation of H_2 on Au. *Nano Lett.* **2013**, *13*, 240–247.

(8) Yu, S.; Wilson, A. J.; Heo, J.; Jain, P. K. Plasmonic Control of Multi-Electron Transfer and C–C Coupling in Visible-Light-Driven CO2 Reduction on Au Nanoparticles. *Nano Lett.* **2018**, *18*, 2189–2194.

(9) Wang, F.; Li, C.; Chen, H.; Jiang, R.; Sun, L.-D.; Li, Q.; Wang, J.; Yu, J. C.; Yan, C.-H. Plasmonic Harvesting of Light Energy for Suzuki Coupling Reactions. *J. Am. Chem. Soc.* **2013**, *135*, 5588–5601.

(10) Lee, J.; Mubeen, S.; Ji, X.; Stucky, G. D.; Moskovits, M. Plasmonic Photoanodes for Solar Water Splitting with Visible Light. *Nano Lett.* **2012**, *12*, 5014–5019.
(11) Marimuthu, A.; Zhang, J.; Linic, S. Tuning Selectivity in Propylene Epoxidation by Plasmon Mediated Photo-Switching of Cu Oxidation State. *Science* **2013**, *339*, 1590–1593.
(12) Christopher, P.; Xin, H.; Linic, S. Visible-Light-Enhanced Catalytic Oxidation Reactions on Plasmonic Silver Nanostructures. *Nat. Chem.* **2011**, *3*, 467–472.
(13) Carretero-Palacios, S.; Jiménez-Solano, A.; Míguez, H. Plasmonic Nanoparticles as Light-Harvesting Enhancers in Perovskite Solar Cells: A User's Guide. *ACS Energy Lett.* **2016**, *1*, 323–331.
(14) Jang, Y. H.; Jang, Y. J.; Kim, S.; Quan, L. N.; Chung, K.; Kim, D. H. Plasmonic Solar Cells: From Rational Design to Mechanism Overview. *Chem. Rev.* **2016**, *116*, 14982–15034.
(15) Wang, Q.; Domen, K. Particulate Photocatalysts for Light-Driven Water Splitting: Mechanisms, Challenges, and Design Strategies. *Chem. Rev.* **2020**, *120*, 919–985.
(16) Le Ru, E. C.; Etchegoin, P. G. Single-Molecule Surface-Enhanced Raman Spectroscopy. *Annu. Rev. Phys. Chem.* **2012**, *63*, 65–87.
(17) Saha, K.; Agasti, S. S.; Kim, C.; Li, X.; Rotello, V. M. Gold Nanoparticles in Chemical and Biological Sensing. *Chem. Rev.* **2012**, *112*, 2739–2779.
(18) Mayer, K. M.; Hafner, J. H. Localized Surface Plasmon Resonance Sensors. *Chem. Rev.* **2011**, *111*, 3828–3857.
(19) Aragay, G.; Pons, J.; Merkoçi, A. Recent Trends in Macro-, Micro-, and Nanomaterial-Based Tools and Strategies for Heavy-Metal Detection. *Chem. Rev.* **2011**, *111*, 3433–3458.
(20) Yadid, M.; Feiner, R.; Dvir, T. Gold Nanoparticle-Integrated Scaffolds for Tissue Engineering and Regenerative Medicine. *Nano Lett.* **2019**, *19*, 2198–2206.
(21) Huang, X.; Jain, P. K.; El-Sayed, I. H.; El-Sayed, M. A. Plasmonic Photothermal Therapy (PPTT) Using Gold Nanoparticles. *Lasers Med. Sci.* **2007**, *23*, 217.
(22) Huang, X.; El-Sayed, I. H.; Qian, W.; El-Sayed, M. A. Cancer Cell Imaging and Photothermal Therapy in the Near-Infrared Region by Using Gold Nanorods. *J. Am. Chem. Soc.* **2006**, *128*, 2115–2120.
(23) Liang, C.; Lu, Z.-A.; Wu, J.; Chen, M.-X.; Zhang, Y.; Zhang, B.; Gao, G.-L.; Li, S.; Xu, P. Recent Advances in Plasmon-Promoted Organic Transformations Using Silver-Based Catalysts. *ACS Appl. Mater. Interfaces* **2020**, *12*, 54266–54284.
(24) Christopher, P.; Moskovits, M. Hot Charge Carrier Transmission from Plasmonic Nanostructures. *Annu. Rev. Phys. Chem.* **2017**, *68*, 379–398.
(25) Boerigter, C.; Aslam, U.; Linic, S. Mechanism of Charge Transfer from Plasmonic Nanostructures to Chemically Attached Materials. *ACS Nano* **2016**, *10*, 6108–6115.
(26) Boerigter, C.; Campana, R.; Morabito, M.; Linic, S. Evidence and Implications of Direct Charge Excitation as the Dominant Mechanism in Plasmon-Mediated Photocatalysis. *Nat. Commun.* **2016**, *7*, 10545.
(27) Ma, J.; Wang, Z.; Wang, L.-W. Interplay between Plasmon and Single-Particle Excitations in a Metal Nanocluster. *Nat. Commun.* **2015**, *6*, 1–11.
(28) Zhang, R.; Bursi, L.; Cox, J. D.; Cui, Y.; Krauter, C. M.; Alabastri, A.; Manjavacas, A.; Calzolari, A.; Corni, S.; Molinari, E.; et al. How To Identify Plasmons from the Optical Response of Nanostructures. *ACS Nano* **2017**, *11*, 7321–7335.
(29) Bernadotte, S.; Evers, F.; Jacob, C. R. Plasmons in Molecules. *J. Phys. Chem. C* **2013**, *117*, 1863–1878.
(30) Zohar, N.; Chuntonov, L.; Haran, G. The Simplest Plasmonic Molecules: Metal Nanoparticle Dimers and Trimers. *J. Photochem. Photobiol. C Photochem. Rev.* **2014**, *21*, 26–39.
(31) Guidez, E. B.; Aikens, C. M. Plasmon Resonance Analysis with Configuration Interaction. *Phys. Chem. Chem. Phys.* **2014**, *16*, 15501–15509.

(32) Guidez, E. B.; Aikens, C. M. Quantum Mechanical Origin of the Plasmon: From Molecular Systems to Nanoparticles. *Nanoscale* **2014**, *6*, 11512–11527.
(33) Wu, Q.; Zhou, L.; Schatz, G. C.; Zhang, Y.; Guo, H. Mechanistic Insights into Photocatalyzed H_2 Dissociation on Au Clusters. *J. Am. Chem. Soc.* **2020**, *142*, 13090–13101.
(34) Zhang, Y.; Nelson, T.; Tretiak, S.; Guo, H.; Schatz, G. C. Plasmonic Hot-Carrier-Mediated Tunable Photochemical Reactions. *ACS Nano* **2018**, *12*, 8415–8422.
(35) Hull, O. A.; Lingerfelt, D. B.; Li, X.; Aikens, C. M. Electronic Structure and Nonadiabatic Dynamics of Atomic Silver Nanowire–N_2 Systems. *J. Phys. Chem. C* **2020**, *124*, 20834–20845.
(36) Yan, L.; Ding, Z.; Song, P.; Wang, F.; Meng, S. Plasmon-Induced Dynamics of H_2 Splitting on a Silver Atomic Chain. *Appl. Phys. Lett.* **2015**, *107*, 083102.
(37) Zhang, Y.; Yan, L.; Guan, M.; Chen, D.; Xu, Z.; Guo, H.; Hu, S.; Zhang, S.; Liu, X.; Guo, Z.; et al. Indirect to Direct Charge Transfer Transition in Plasmon-Enabled CO_2 Photoreduction. *Adv. Sci.* **2022**, *9*, 2102978.
(38) Kumar, P. V.; Rossi, T. P.; Kuisma, M.; Erhart, P.; Norris, D. J. Direct Hot-Carrier Transfer in Plasmonic Catalysis. *Faraday Discuss.* **2019**, *214*, 189–197.
(39) Rossi, T. P.; Kuisma, M.; Puska, M. J.; Nieminen, R. M.; Erhart, P. Kohn–Sham Decomposition in Real-Time Time-Dependent Density-Functional Theory: An Efficient Tool for Analyzing Plasmonic Excitations. *J. Chem. Theory Comput.* **2017**, *13*, 4779–4790.
(40) Libisch, F.; Cheng, J.; Carter, E. A. Electron-Transfer-Induced Dissociation of H_2 on Gold Nanoparticles: Excited-State Potential Energy Surfaces via Embedded Correlated Wavefunction Theory. *Z. Für Phys. Chem.* **2013**, *227*, 1455–1466.
(41) Gieseking, R. L. M. Plasmons: Untangling the Classical, Experimental, and Quantum Mechanical Definitions. *Mater. Horiz.* **2022**, *9*, 25–42.
(42) Dillon, A. D.; Gieseking, R. L. M. Evolution of Plasmon-like Excited States in Silver Nanowires and Nanorods. *J. Chem. Phys.* **2022**, *156*, 074301.
(43) Rohrdanz, M. A.; Martins, K. M.; Herbert, J. M. A Long-Range-Corrected Density Functional That Performs Well for Both Ground-State Properties and Time-Dependent Density Functional Theory Excitation Energies, Including Charge-Transfer Excited States. *J. Chem. Phys.* **2009**, *130*, 054112.
(44) Hay, P. J.; Wadt, W. R. Ab Initio Effective Core Potentials for Molecular Calculations. Potentials for the Transition Metal Atoms Sc to Hg. *J. Chem. Phys.* **1985**, *82*, 270–283.
(45) Hay, P. J.; Wadt, W. R. Ab Initio Effective Core Potentials for Molecular Calculations. Potentials for K to Au Including the Outermost Core Orbitals. *J. Chem. Phys.* **1985**, *82*, 299–310.
(46) Wadt, W. R.; Hay, P. J. Ab Initio Effective Core Potentials for Molecular Calculations. Potentials for Main Group Elements Na to Bi. *J. Chem. Phys.* **1985**, *82*, 284–298.
(47) Rabilloud, F. Description of Plasmon-like Band in Silver Clusters: The Importance of the Long-Range Hartree-Fock Exchange in Time-Dependent Density-Functional Theory Simulations. *J. Chem. Phys.* **2014**, *141*, 144302.
(48) Rabilloud, F. Assessment of the Performance of Long-Range-Corrected Density Functionals for Calculating the Absorption Spectra of Silver Clusters. *J. Phys. Chem. A* **2013**, *117*, 4267–4278.
(49) Silverstein, D. W.; Jensen, L. Assessment of the Accuracy of Long-Range Corrected Functionals for Describing the Electronic and Optical Properties of Silver Clusters. *J. Chem. Phys.* **2010**, *132*, 194302.
(50) Moore, J. E.; Morton, S. M.; Jensen, L. Importance of Correctly Describing Charge-Transfer Excitations for Understanding the Chemical Effect in SERS. *J. Phys. Chem. Lett.* **2012**, *3*, 2470–2475.

(51) Frisch, M. J.; Trucks, G. W.; Schlegel, H. B.; Scuseria, G. E.; Robb, M. A.; Cheeseman, J. R.; Scalmani, G.; Barone, V.; Petersson, G. A.; Nakatsuji, H., et al. *Gaussian 16*, Revision C.01; Gaussian, Inc.: Wallingford, CT, 2016.
(52) Li, X.; Govind, N.; Isborn, C.; DePrince, A. E.; Lopata, K. Real-Time Time-Dependent Electronic Structure Theory. *Chem. Rev.* **2020**, *120*, 9951–9993.
(53) Li, X.; Tully, J. C.; Schlegel, H. B.; Frisch, M. J. Ab Initio Ehrenfest Dynamics. *J. Chem. Phys.* **2005**, *123*, 084106.
(54) Kar, T.; Sannigrahi, A. B. Effect of Basis Set on Mulliken and Löwdin Atomic Charges, Bond Orders and Valencies of Some Polar Molecules. *J. Mol. Struct. THEOCHEM* **1988**, *165*, 47–54.
(55) Habteyes, T. G. Anions as Intermediates in Plasmon Enhanced Photocatalytic Reactions. *J. Phys. Chem. C* **2020**, *124*, 26554–26564.

TOC Graphic

